

Supporting Information for:

Synthetic macrocycle nanopore for potassium-selective transmembrane transport

Dan Qiao^{1#}, Himanshu Joshi^{2#}, Huangtianzhi Zhu³, Fushi Wang¹, Yang Xu¹, Jia Gao¹,
Feihe Huang^{3,4}, Aleksei Aksimentiev^{2*} and Jiandong Feng^{1*}

*¹Laboratory of Experimental Physical Biology, Department of Chemistry, Zhejiang University,
Hangzhou 310027, China*

²Department of Physics, University of Illinois at Urbana-Champaign, Urbana IL, 61801, USA

*³State Key Laboratory of Chemical Engineering, Key Laboratory of Excited-State Materials of
Zhejiang Province, Stoddart Institute of Molecular Science, Department of Chemistry, Zhejiang
University, Hangzhou 310027, China*

⁴ZJU-Hangzhou Global Scientific and Technological Innovation Center, Hangzhou, 311215, China

Table of contents

- 1. Chemical synthesis and characterization of EPM nanopores**
- 2. Experimental setup, ion transport measurements and methods**
- 3. Geometry optimization of EPM structures**
- 4. All-atom MD simulations of water and ion transport through EPM nanopores**
- 5. Supporting discussions and figures**
- 6. Supporting movie legends**
- 7. Supporting references**

1. Chemical synthesis and characterization of EPM nanopores

The synthesis of the EPM was carried out by adapting the method published elsewhere¹ and the side chain with 4 Phe groups was modified at the eight sites of the molecule². Detailed synthetic route is sheched in **Figure S1-2**. The corresponding compounds were prepared using the following approach,

Synthesis of compound 1: A solution of 4,4'-bis(chloromethyl)-1,1'-biphenyl (0.4 g, 1.6 mmol) and 1,4-diethoxybenzene (1.6 g, 9.6 mmol) in 150 mL of DCM was added to AlCl₃ (0.26 g, 2.0 mmol). The mixture was stirred at room temperature for 2 h and then quenched with water. The organic phase was separated and concentrated to obtain the crude product, which was further purified on column chromatography using hexane: ethyl acetate = 20 : 1 as the eluent. The pure product (0.26 g, yield 32%) was acquired as a white solid after recrystallization in CHCl₃/MeOH, and followed by NMR characterizations showing ¹H NMR (400 MHz, CDCl₃, 298 K) δ 7.46 (d, J = 8.1 Hz, 4H), 7.28 (s, 4H), 6.75 (s, 2H), 6.70 (d, J = 4.5 Hz, 4H), 3.96 (m, J = 1.9 Hz, 12H), 1.36 (m, J = 4.1 Hz, 12H).

Synthesis of compound 2: Compound **1** (1.0 g, 2.0 mmol) and paraformaldehyde (0.32 g, 10 mmol) were stirred in 100 mL of CHCl₃, and then 1.0 mL of BF₃•OEt₂ was injected. The mixture was stirred at room temperature and monitored on TLC. 400 mL of methanol was added to quench the reaction. The precipitate was filtered and purified on column chromatography using hexane: DCM = 1: 4 as eluent to obtain the pure product as a white solid (114 mg, yield 11 %). The NMR result: ¹H NMR (400 MHz, CDCl₃, 298 K) δ 7.35 (d, J = 8.1 Hz, 8H), 7.20 (d, J = 8.1 Hz, 8H), 6.93 (s, 4H), 6.66

(s, 4H), 3.92 (ddd, $J = 17.2, 13.7, 6.7$ Hz, 28H), 1.41 (t, $J = 6.9$ Hz, 12H), 1.28 (t, $J = 6.9$ Hz, 12H).

Synthesis of compound **3**: Under the protection of argon, 114 mg of compound **2** was dissolved in 20 mL of CHCl_3 and then excess BBr_3 was added. The mixture was stirred overnight and poured into water. The precipitate was filtered and used in the next step without further purification.

Synthesis of compound **4**: Under the protection of argon, hydroxyl macrocycle **3**, K_2CO_3 (2.8 g, 20 mmol) and ethyl 2-bromoacetate (3.3 g, 20 mmol) were dissolved in 40 mL of acetonitrile. The mixture was refluxed for 3 days. After cooling to room temperature, the suspension was filtered, and the filtrate was concentrated. The crude product was purified on column chromatography using DCM: ethyl acetate = 10: 1 as eluent to get the pure product as white solid (92 mg, 2 steps yield 56%). NMR identification result: ^1H NMR (400 MHz, CDCl_3) δ 7.34 (s, 8H), 7.28 (s, 8H), 7.24 (s, 4H), 6.59 (s, 4H), 4.57 (d, $J = 17.5$ Hz, 16H), 4.26 (d, $J = 7.1$ Hz, 8H), 4.19 (d, $J = 7.1$ Hz, 8H), 4.00 (s, 12H), 1.27 (s, 12H), 1.22 (s, 12H).

Synthesis of compound **5**: Compound **4** (92 mg, 0.06 mmol) was suspended in a 1:1 mixture of water/EtOH (10 mL). After adding 80 mg of NaOH (2.0 mmol), the mixture was refluxed overnight. The homogeneous solution was poured into HCl (aq., 10 mL); white precipitate formed and was filtered to obtain compound **5**. NMR identification: ^1H NMR (400 MHz, DMSO, 298 K) δ 7.33 (d, $J = 8.2$ Hz, 8H), 7.23 (d, $J = 8.3$ Hz, 8H), 7.18 (s, 4H), 6.79 (s, 4H), 4.58 (d, $J = 14.6$ Hz, 16H), 3.84 (d, $J = 24.8$ Hz, 16H).

Synthesis of compound **6**: Compound **5** (42 mg), H₂N-Phe-Phe-Phe-Phe-OEt (350 mg), DMAP (300 mg) and EDC•HCl (130 mg) were suspended in 5.0 mL of DMF. The suspension was stirred at 50°C for 24 h. To obtain the crude product, the suspension was poured into HCl (30 mL) in order to dissolve EDC and DMAP. The peptide-substituted macrocycle (11 mg) was filtered and dried. Due to the multiple amide bonds, compound **6** cannot be fully purified by conventional methods and the mixture was used directly in the following experiments. The result of MALDI-TOF mass indicates compound **6** was successfully prepared: the calculated molecular weight is 6214.91 and the found molecular weight is 6212.52. Other peaks in MALDI-TOF spectrum may be ascribed to partly peptide-substituted macrocycles and amide hydrolysis.

2. Experimental setup, ion transport measurements and methods

Nanopore Experiments: 1 mg of EPM molecules was added to 10 mL DI (Milli-Q) water then ultrasonically dissolved and the undissolved matter was filtered out. The clarified solution served as the stock solution in our experiments. 3 mg (30 mg/ml) DPhPC (Avanti Polar Lipids, cat. no. 850356P) with 10 wt% Cholesterol were dissolved in decane³. The lipid solution can be stored at 4°C up to one week. 1 µL of the lipid solution was pipetted onto the tip of the No. 000 brush and we then spread the solution evenly on both sides of the hole of the Delrin perfusion cup (Warner Instruments, cat. no. 64-0427) until the aperture was evenly covered. 1 mL electrolyte solution was pipetted into each chamber. Two Ag/AgCl electrodes were then immersed in the solutions of the *cis* and *trans* chambers. Lipid bilayer formation was confirmed by either measuring the membrane capacitance system (estimated bilayer capacitance in the range of 40-70 pF) or checking the membrane stability under a voltage of 300-400 mV⁴. The EPM stock solution diluted by 10 times with DI (Milli-Q) water was followed by adding of 1 wt% a nonionic surfactant (Polyethylene Glycol Monooleyl Ether n(=):10, TCI, P0714-25G)⁵. A negative electric potential (-180 mV) was applied and 20-30 µL of diluted EPM solution was added to a region near the supporting hole in the *cis* chamber (ground side). This step was repeated if no current jump was observed in 20 minutes. Current data recording was filtered through a 2 kHz low-pass Bessel filter and digitized with a Digidata 1550B converter (equipped with Axonpatch 200B amplifier, Molecular Devices) at a sampling frequency of 10 kHz, unless otherwise stated. The voltage was reduced to -100 mV once the current jump occurred,

because the high potential of -180 mV may lead to a possible second molecular insertion. Current-voltage curves for different concentrations and pH of potassium chloride and sodium chloride were measured accordingly. Reverse potential was measured by using a concentration gradient configuration as described in **Figure S12**.

Cryo-EM imaging: Lipid vesicles were prepared by using the film rehydration method. 10 mg DPhPC was dissolved in 5 mL chloroform. The solution was dried under high vacuum to remove all solvent, and the resulting film was rehydrated with 5 mL, 500 mM KCl solution for 4 h. After 10 repeated freezing-melting cycles the suspension was extruded through a 0.2 μm PC membrane (Millipore) for 10 cycles to obtain lipid vesicles⁶. The EPM stock solution was added to the vesicles before Cryo-EM experiments. Cryo-EM was performed on a FEI Talos F200C TEM operating at 200 kV. Images were recorded by using a 4 K \times 4 K pixel FEI CETA CMOS camera at a magnification of 120,000 \times giving a pixel size of 0.092 nm. Images were acquired with doses of 661 e/ Å^2 per image^{7, 8}.

3. Geometry optimization of EPM structures

The initial structure of EPM was optimized at B3LYP/6-31+G(d) level of theory without imposing any constraint to the symmetry using density functional theory (DFT) methods in *Gaussian* 16. The calculation was carried out with considering the solvent phase of water using the solvation model based on density (SMD). As the complete side chains of EPM were too large for quantum chemistry calculation, here we only used part of the side chains -OCH₂CONH₂ as the replacement for the full peptide chains.

4. All-atom MD simulations of water and ion transport through EPM

nanopores

All-atom MD simulations were performed using program NAMD⁹, a 2 fs integration time step, 2-2-6 multiple time stepping, periodic boundary conditions and particle mesh Ewald (PME) method over a 1-Å resolution grid to calculate the long range electrostatic interaction¹⁰. The Nose-Hoover Langevin piston¹¹ and Langevin thermostat were used to maintain the constant pressure and temperature in the system. An 8-10-12 Å cutoff scheme was used to calculate van der Waals and short-range electrostatic forces. SETTLE algorithm¹² was applied to keep water molecules rigid whereas RATTLE algorithm¹³ constrained all other covalent bonds involving hydrogen atoms. CHARMM36 force field parameters described the bonded and non-bonded interactions among channel, membrane, water and ions^{14, 15}. The topology and force-field parameters for the constriction of the EPM channel (excluding eight covalently attached Phe side chains) were obtained using the CHARMM General Force Field (CGenFF) webserver¹⁶. CHARMM36 was used for the Phe side chains. Custom non-bonded fix (NBFIX) corrections were applied to improve the description of non-bonded interaction between the lipid headgroup and ions¹⁷. The coordinates of the system were saved at an interval of 20 ps. The visualization, analysis and post processing the simulation trajectories were performed using VMD¹⁸ and CPPTRAJ¹⁹.

The initial PDB structure of the pillararene molecules was obtained by modifying the structure published elsewhere¹ with 4 Phe groups as side chains. Phe peptides were attached to the pillararene core according to the chemical structure of the EPM pore

using a custom psfgen script. **Supporting Movie 1** shows a 3D rotating view of the EPM nanopore. After aligning the symmetry axis of EPM channel with the z axis, the EPM molecule was embedded into a $10.6 \times 10.6 \text{ nm}^2$ patch of pre-equilibrated POPC lipid bilayer membrane, placing the EPM constriction within the midplane of the lipid membrane. The lipid patch was generated using the CHARMM-GUI membrane builder²⁰ and pre-equilibrated for approximately 400 ns. Lipid molecules that overlapped with the channel were removed. The resulting systems were solvated with TIP3P water molecules²¹ using the Solvate plugin of VMD¹⁸. Potassium and chloride ions were added to 1 M concentration using the Autoionize plugin of VMD. The final assembled system measured $11 \times 11 \times 9 \text{ nm}^3$ and contained approximately 98,000 atoms.

Following the assembly, the system underwent 1200 steps of energy minimization using the conjugate gradient method to remove steric clashes. After energy minimization, the system was subjected to a 20 ns equilibration at a constant number of atoms (N), pressure ($P = 1 \text{ bar}$) and temperature ($T = 300 \text{ K}$), the NPT ensemble, with harmonic restraints applied to all non-hydrogen atoms of EPM molecule. The restraints were applied relative to the initial coordinates of the atoms, each with a spring constants $k_1 = 1 \text{ kcal mol}^{-1} \text{ \AA}^{-2}$. For the next 20 ns, the harmonic restraints were reduced to $k_2 = 0.1 \text{ kcal mol}^{-1} \text{ \AA}^{-2}$. After 40 ns, the harmonic restraints were removed from all peptide side chains and the system was equilibrated for 215 ns using $0.1 \text{ kcal mol}^{-1} \text{ \AA}^{-2}$ harmonic restraints applied only to the non-hydrogen atom of the EPM constriction. Finally, all the harmonic restraints were released completely, and the system was

simulated for 300 ns in the absence of any restraints.

For our replica exchange umbrella sampling (REUS) simulations of the single ion PMF, we constructed several simulation systems each containing an atomic model of the EPM channel constriction (excluding peptide side chains) submerged in a $4 \times 4 \times 4$ nm³ volume of electrolyte solution (either 1 M KCl or 1 M NaCl), a system of approximately 6,000 atoms. As initial coordinates of the EPM channel constriction, we used either the DFT optimized structure (see **SI Section 3** and **Figure S15**) or the X-Ray structures¹. The PMFs were computed for both structures and the following two harmonic restraints conditions: (1) restraining all non-hydrogen atoms of the constriction to their initial coordinate, each with a spring constant of 5 kcal mol⁻¹ Å⁻², and (2) restraining only the four carbon atoms, two at each end of the pillararene constriction (light green spheres in **Figure 4g**) using the same spring constant. Each system underwent a 10 ns of NPT equilibration simulation. Following that, steered molecular dynamics method (SMD)^{22, 23} was used to move one cation along the *z*-axis from -10 to 10 Å in 5 ns through the center of the channel. The SMD simulation trajectory was used to create 41 copies of the system differing by the *z*-coordinate of the respective ion, one system for each 0.5 Å sampling window along the *z*-axis. Each replica was simulated for 50 ns having the *z*-coordinate of the ion restrained to the center of the sampling window with the spring constant of 2.5 kcal mol⁻¹ Å⁻². In addition, the “distanceXY” colvar restrain (of 3 Å radius) was applied to make sure that the ion samples conformations within the constriction of the EPM molecule. During the simulation, the replicas were allowed to exchange the biasing potential between the

neighboring windows with a probability given by the Metropolis algorithm. Finally, WHAM²⁴ was used to subtract the contribution from the confining harmonic potential and extract the PMF of the ion along the z -axis.

5. Supporting discussions and figures

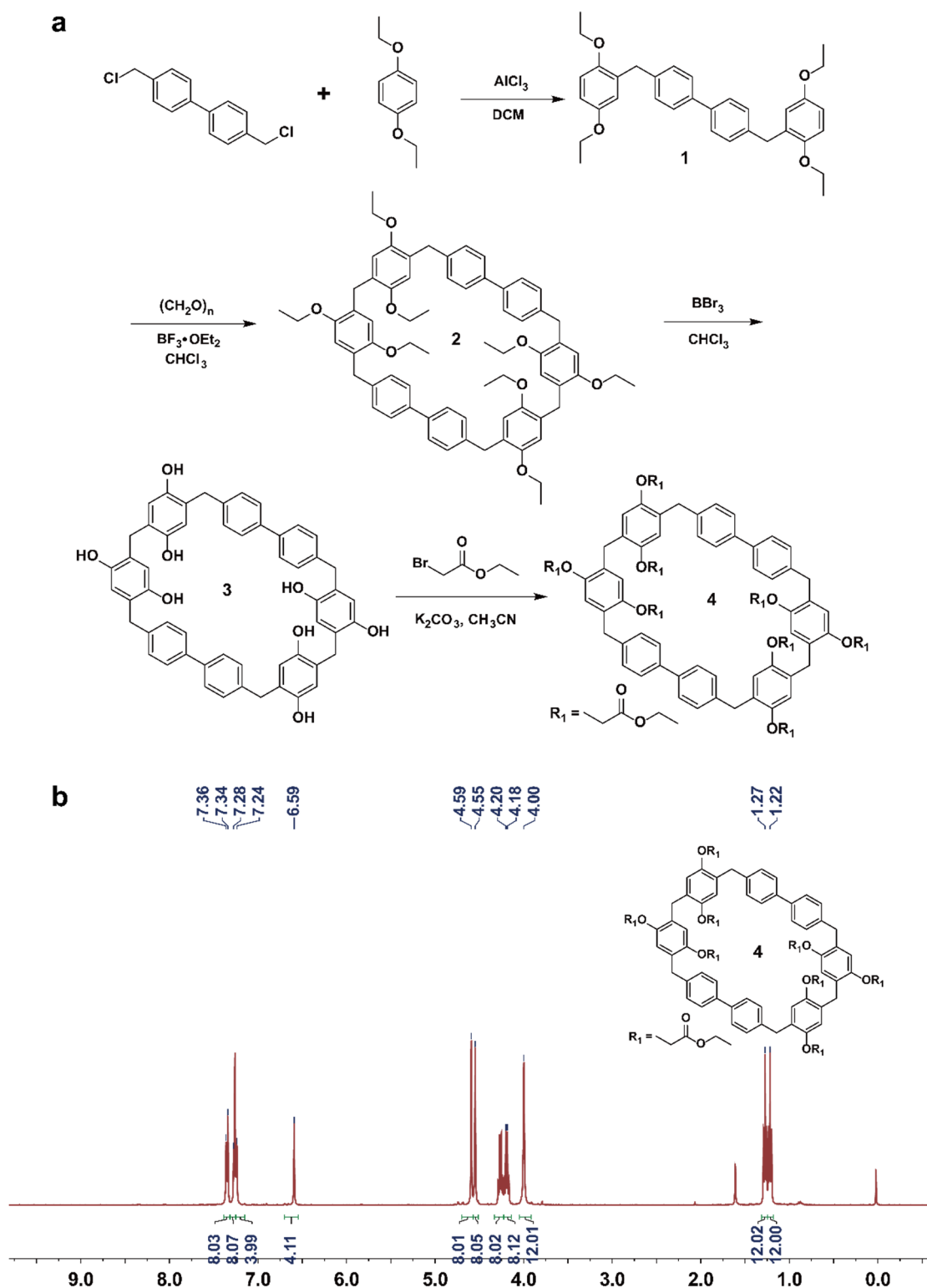


Figure S1. Synthetic route for compounds 1-4. a. Synthetic route of compound 4. b.

^1H NMR (400 MHz, CDCl_3 , 298 K) of compound 4.

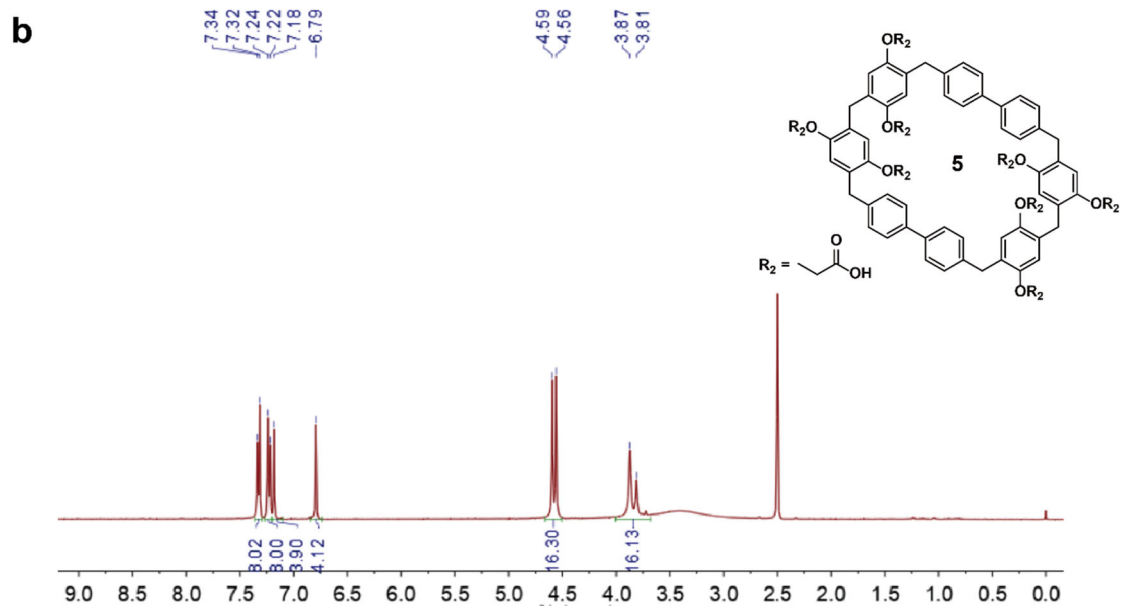
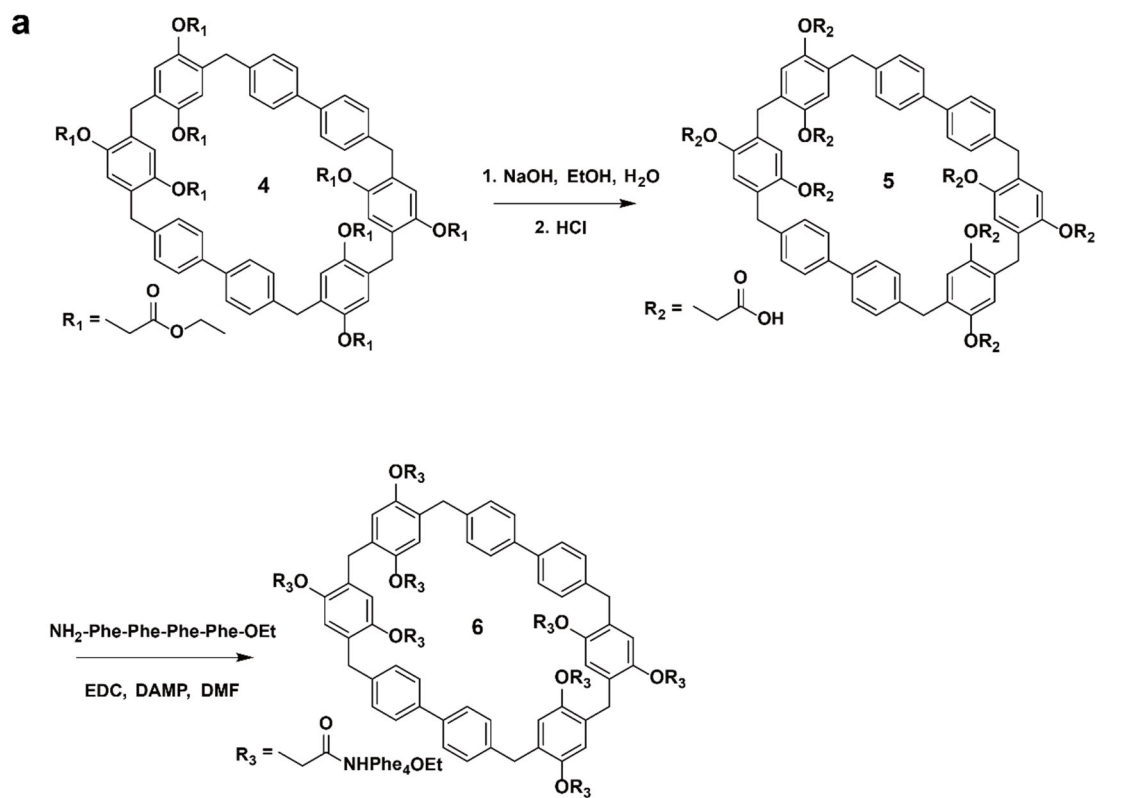


Figure S2. Synthetic route for compound 4-6. a. Synthetic route of compound 6 (EPM). b. ^1H NMR (400 MHz, CDCl_3 , 298 K) of compound 5.

Design of EPM pores: Compound 5 (Figure S2a) presents a hydrophobic cavity of 14 Å \times 6 Å diameter, which is suitable to accommodate ions. Therefore, the EPM was built by choosing compound 5 (Figure S2a) as the foundational unit and Phe peptides as the side chains. The terminal esterified chains have good amphiphile capability, and the nonpolar benzyl group of Phe and the terminal ester group on the peptide chains can increase the membrane-insertion capability of EPM, which facilitates the stability of formed transmembrane EPM nanopores in the lipid bilayer. In addition, compared with the 3 Phe peptides, 4 Phe side chain is better to support the single transmembrane EPM in lipid bilayer because the pillararene derivatives can form long self-assembled nanotubes if the peptide chain is too short^{2, 25}. Meanwhile, the EPM with the rigid biphenyl unite is also restrained to form the barreled molecular structures^{1, 2, 25}.

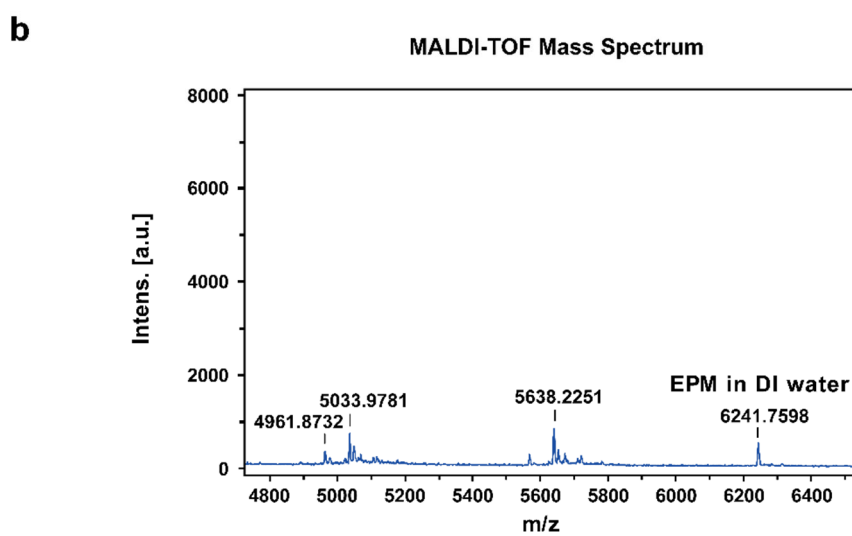
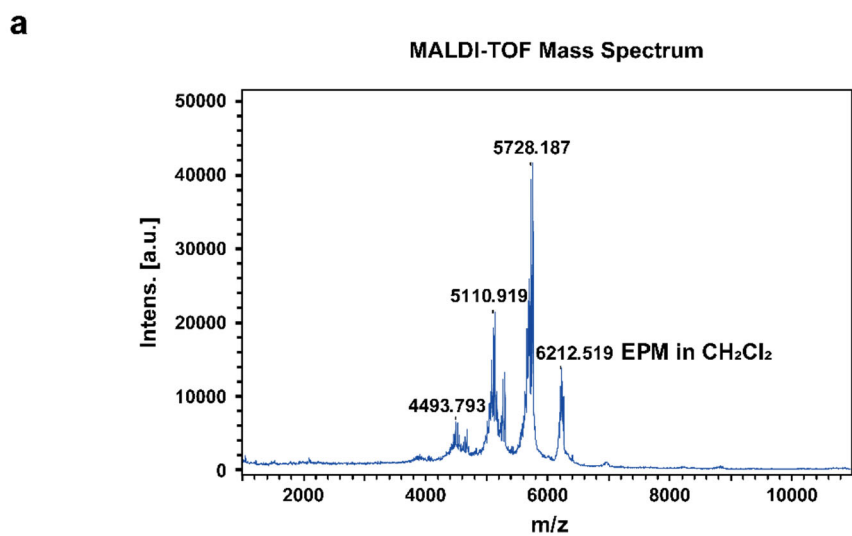


Figure S3. MALDI-TOF mass spectra of the EPM pores. a. Solvent: CH₂Cl₂. **b.** Stock EPM solution. Solvent: DI water. The value of m/z in **b.** is slightly different from **a.** because EPM aqueous solution may allow hydrolyzed or ionized sites.

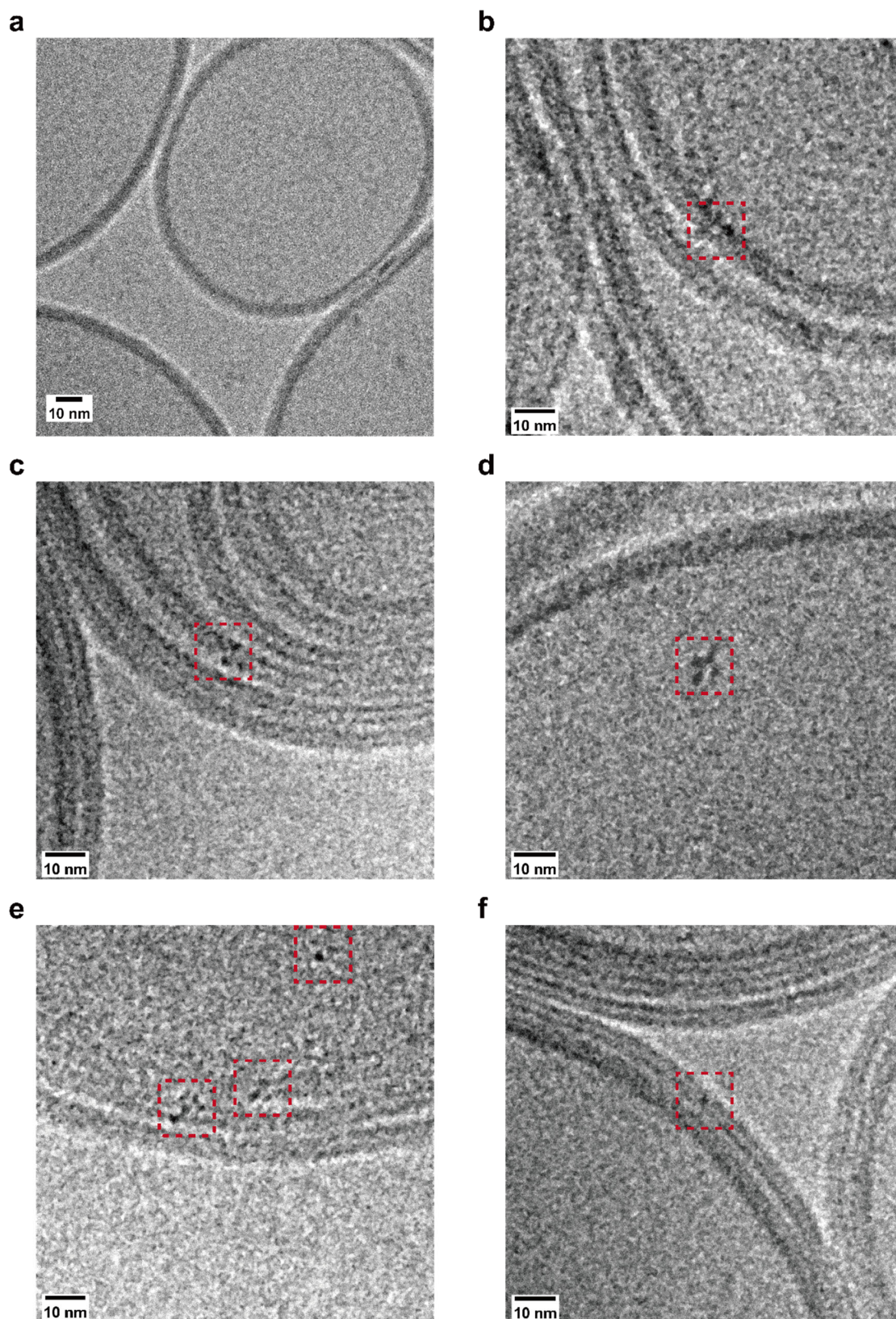


Figure S4. Cryo-EM of EPM nanopore on lipid vesicles. a. Image of lipid bilayer without EPM. **b-f.** Cryo-EM images of EPM incorporated lipid vesicles.

Formed transmembrane EPM pore: Although our ionic transport measurement clearly indicates the formation of single nanopores, it does not rule out the possibility that the formed single nanopores are from EPM aggregates instead of the monomers of EPM molecules. Knowing the exact spatial arrangements of these pores in the lipid membrane is currently challenging due to a lack of experimental techniques and their resolution but we did not observe EPM aggregation in lipid bilayer in Cryo-EM experiments with EPM incorporated lipid vesicles (>100 images). Despite the inadequacy in offering good resolution directly probing the entire structure of a single EPM, Cryo-EM can easily identify the EPM aggregate (larger nanotubes or crosslinked structures) without concession but the result does not suggest such aggregations. Here we also listed some TEM images that may contain single EPM molecules in lipid vesicles (**Figure S4**). The Cryo-EM result suggests that the EPM molecule has the possibility of inserting into the phospholipid bilayer to form transmembrane channel. Moreover, the MALDI-TOF result of EPM in water shows that there was no aggregation formed in aqueous solution for the diluted solution that we used (**Figure S16-18**).

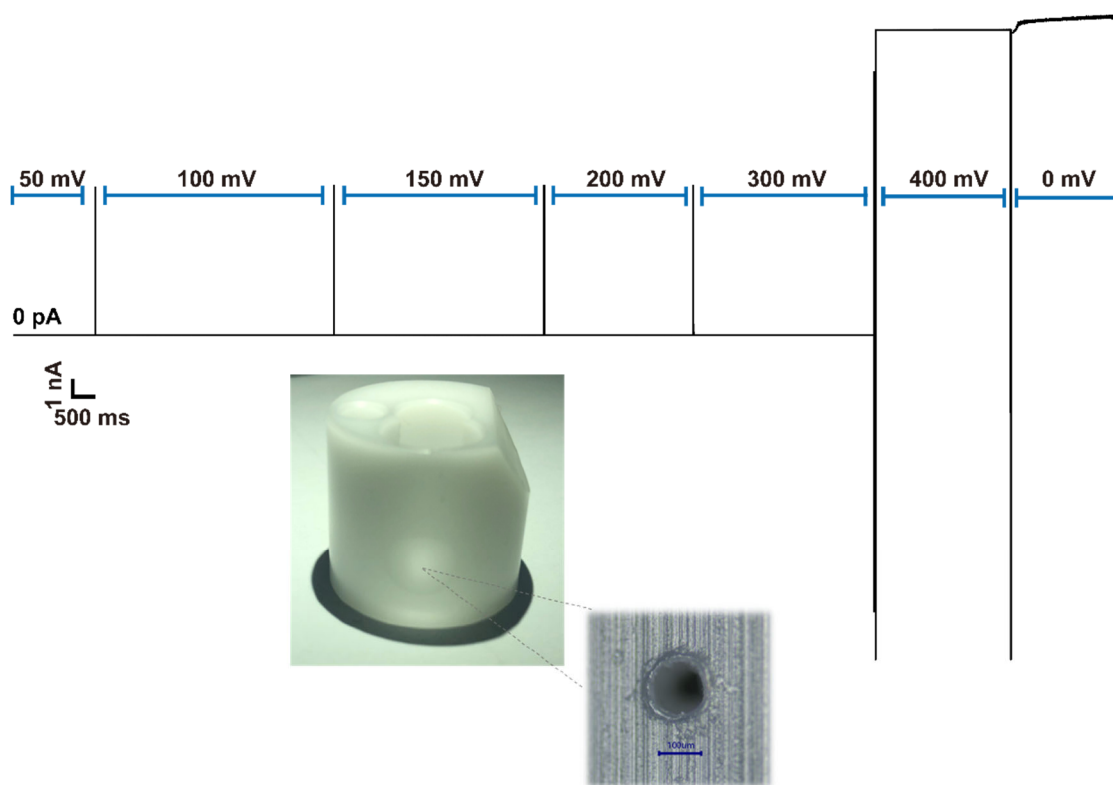


Figure S5. Current trace of lipid bilayer membrane under different voltage. This result shows the breaking of the formed lipid bilayer membrane by using a high voltage in the range of 300 mV – 400 mV.

Stability: The lipid bilayer capacitance is between 40 pF and 70 pF and can be easily broken by a voltage of 300 to 400 mV. Both ways can be used to check the formed single bilayer²⁶. Compared with solid state nanopores, lipid bilayer is more fragile and less stable²⁷, which is also an important factor affecting the stability of formed membrane nanopores. On the other hand, the noise of transmembrane nanopore formed in lipid bilayer is generally lower than the noise of solid state nanopores^{4, 28, 29}.

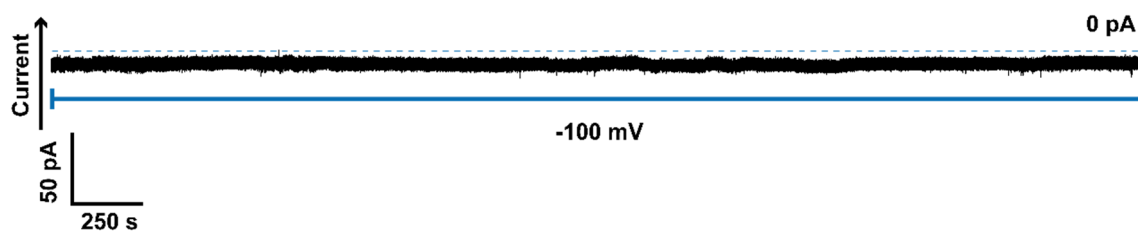


Figure S6. Stability of EPM nanopores for ion transport measurements. The current trace of a single stable EPM nanopore in 500 mM KCl solution, biased at -100 mV. The total length of time is 1 h.

The current trace shows that EPM transmembrane nanopores can be stably recorded up to 1 h, comparable to the stability of typical biological nanopores. The stable measurements address the main issues in conventional electric measurements for the reported sythetic small-molecule channels that are usually diffucult to form stable channels or pores³⁰⁻³⁴.

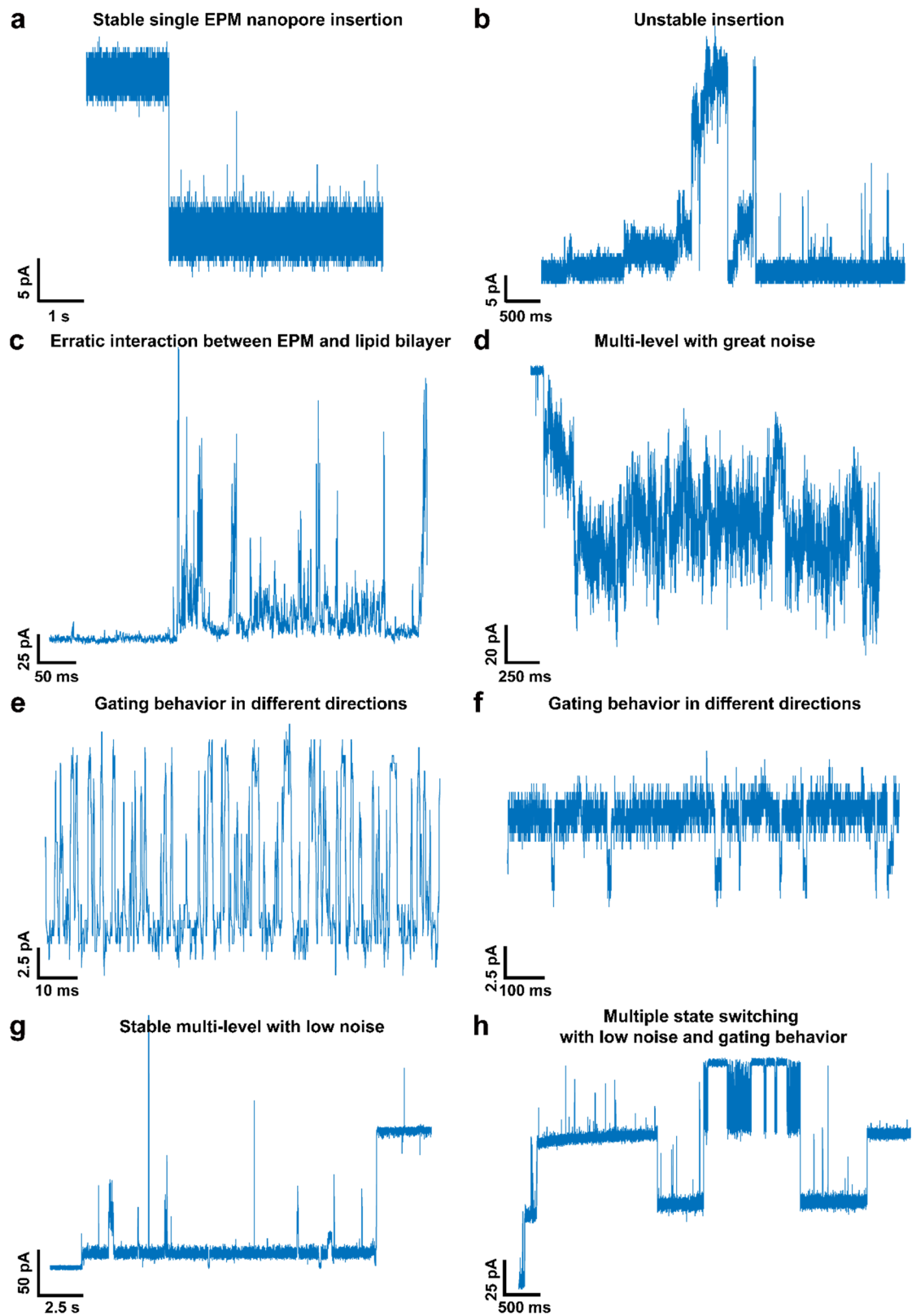


Figure S7. Various current traces of EPM pores observed in the experiments. a-h.

Examples of pore insertion events.

Stable pore insertion: An example current trace is shown in **Figure S7a**, which represents that a single EPM molecule is successfully inserted into the lipid membrane to form a stable nanopore. In our initial attempts, there were occasionally other types of observed events, as shown in **Figure S7b** and **c**, with only some transient unstable interactions. Then, cholesterol was added to the lipid solution to strengthen the stability of the lipid bilayer membrane³, and detergent⁵ was added to the stock solution of EPM, resulting in a higher probability of obtaining the stable trace shown in **Figure S7a**. Gating behavior occasionally (~20% of all EPM pores) occurs after the nanopore insertion. As shown in **Figure S7e** and **f**, the direction and opening/closing rate are also stochastic. In addition, in the experiment, multiple EPM molecules (**Figure S7d**, **g**, and **h**) can simultaneously get inserted into the membrane to form multiple nanopores, and the concentration of EPM nanopore should be further decreased. For our experiments, we conducted the subsequent measurements after obtaining the trajectories as shown in **Figure S7a**.

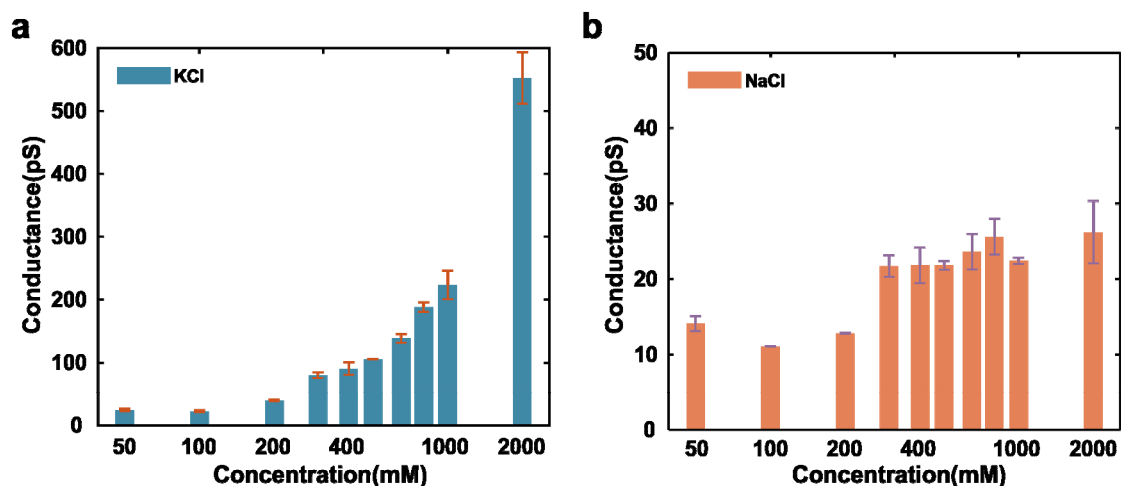


Figure S8. Ionic conductance of single EPM nanopores as a function of concentration. a. KCl solution. **b.** NaCl solution. Error bars are derived from the standard deviation from multiple experimental measurements.

Ionic transport: Ionic conductance of single EPM nanopore versus ion concentrations shows that the transport of potassium ions through EPM pores increases with the increase of ion concentration while there is no significant dependence for sodium ions. Moreover, the concentration dependence confirms that the measured conductance originates from the transport of potassium ions rather than other effects. To quantify this conductance difference, we plotted the ratio between potassium conductance and sodium conductance (main **Figure 3e**), yielding a selectivity factor of 21 at 2 M.

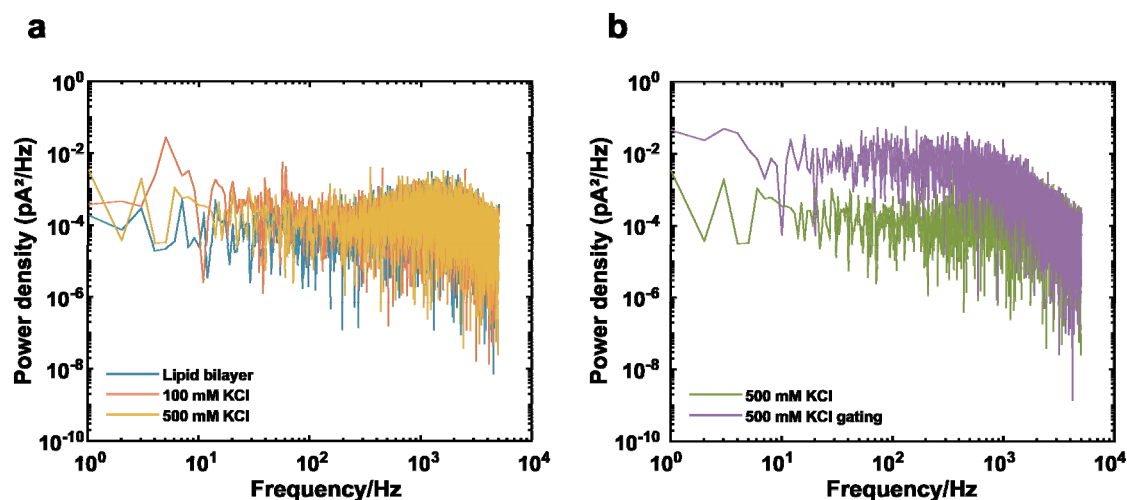


Figure S9. Noise for the EPM nanopores in different conditions. **a.** PSD analysis of the EPM ionic current trace with 100 mM KCl, under - 100 mV (rms = 0.95 pA) and 500 mM KCl, under - 100 mV (rms = 1.03 pA). The lipid bilayer is used as the control (rms = 0.91 pA), under 0 mV. **b.** PSD analysis of the EPM ionic current trace 500 mM KCl with and without gating behavior (rms = 2.9 pA), under + 100 mV.

Noise of EPM nanopores: There are different types of noise sources in a typical nanopore system including low frequency 1/f noise, white noise (~100-2000 Hz) such as shot noise and thermal current noise, dielectric noise (1-10 kHz) and capacitive noise (>10 kHz)^{28, 29}. Our EPM nanopore is constructed on a lipid membrane and its noise is comparable to the noise of other biological nanopore systems such as MspA, α -HL and ReFraC²⁹. PSD analysis of single EPM channel at 100 mM, 500 mM under -100 mV, is shown in **Figure S9a**. The higher frequency (1-10 kHz) noise is mainly contributed to dielectric noise resulted from the loss conductance from the lipid membrane. The used material for membrane supporting hole is Teflon which has a low dielectric constant and dielectric loss ($\epsilon_r = 1.89$ -1.93 and $D = (0.8-2) \times 10^{-4}$, respectively)²⁹ and thereby

the lipid bilayer itself is the main cause of dielectric noise. Potentially, this type of noise can be further reduced by decreasing the area of the supporting hole on Teflon.

Notably, in **Figure S9b**, the PSD becomes much different when a same EPM nanopore switches to its gating state. The significant change in low-frequency $1/f$ noise for gating may originate from the conformational or charge fluctuations of EPM nanopores and the membrane instability, as in other types of biological pores²⁹. The mechanism causing gating in both natural ion channels and artificial channels remains unclear from many aspects. Further experiments and simulations are needed to understand the exact reason leading to the gating behavior.

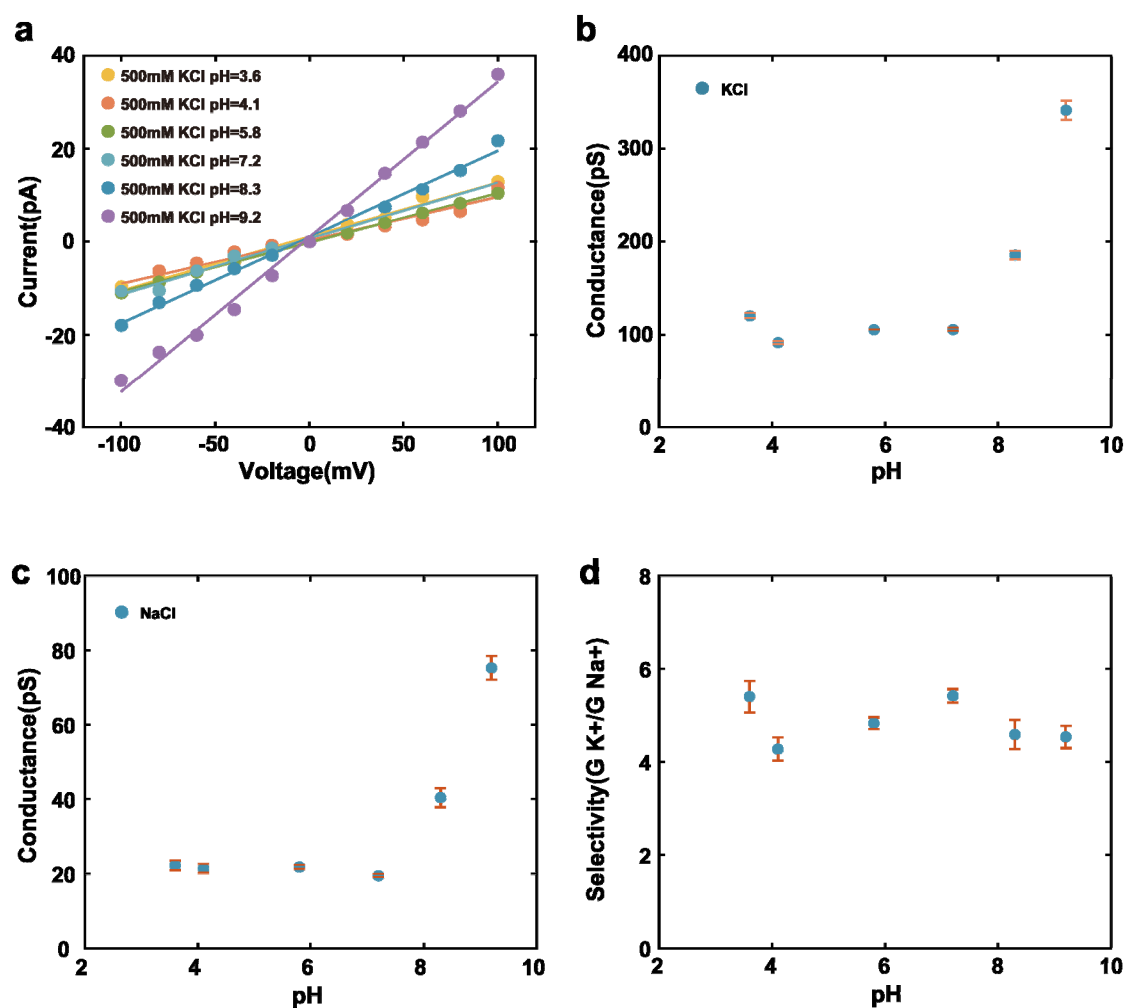


Figure S10. Ionic current measurements in diverse pH of KCl and NaCl solution.

a. *I-V* curves of single EPM nanopore in different pH conditions of 500 mM KCl solution. **b-c.** Conductance of the EPM nanopore as a function of pH values in 500 mM KCl and NaCl solution. **d.** Selectivity of the EPM nanopores as a function of solution pH. The conductance of a single EPM channel was measured by changing the pH of the electrolyte solution. The conductance increases quickly when the pH increases above 8 for both potassium chloride and sodium chloride solution. However, the selectivity of EPM does not considerably change with the change of pH. Error bars are derived from the standard deviation from multiple experimental measurements.

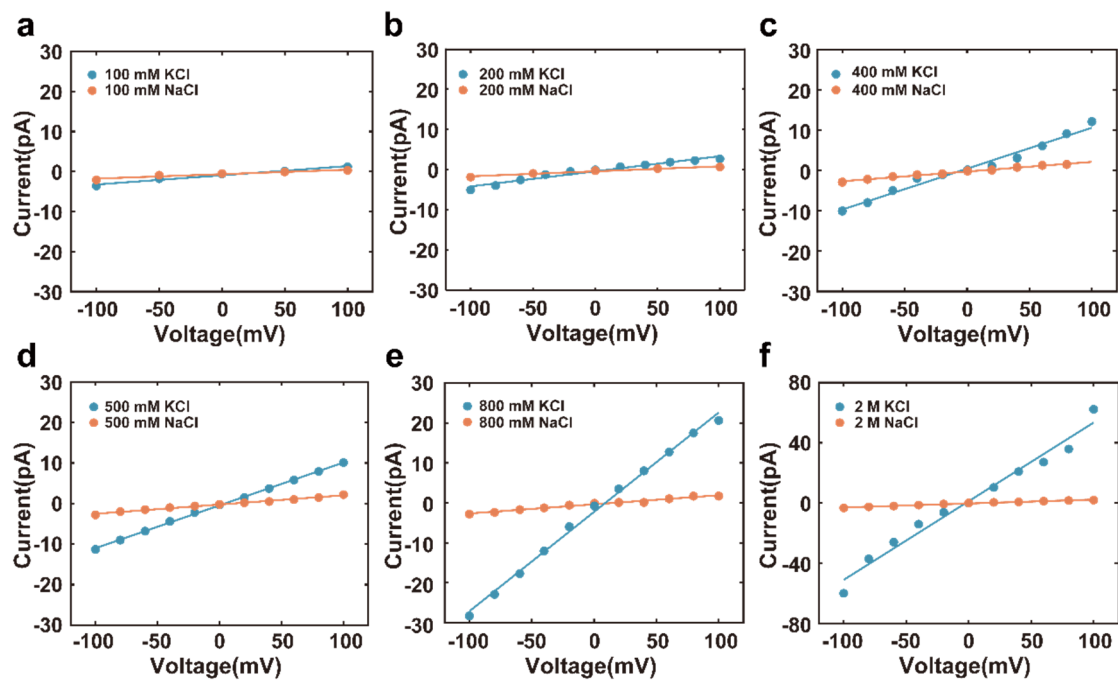


Figure S11. Potassium selective ion transport. a-f. I - V curves of a single EPM nanopore in different concentration solution. Blue: KCl solution. Orange: NaCl solution.

I - V curve measurements: The conductance and selectivity for potassium chloride and sodium chloride solution increase with the increase of concentrations, also indicating that potassium ions are indeed conducted by EPM nanopores.

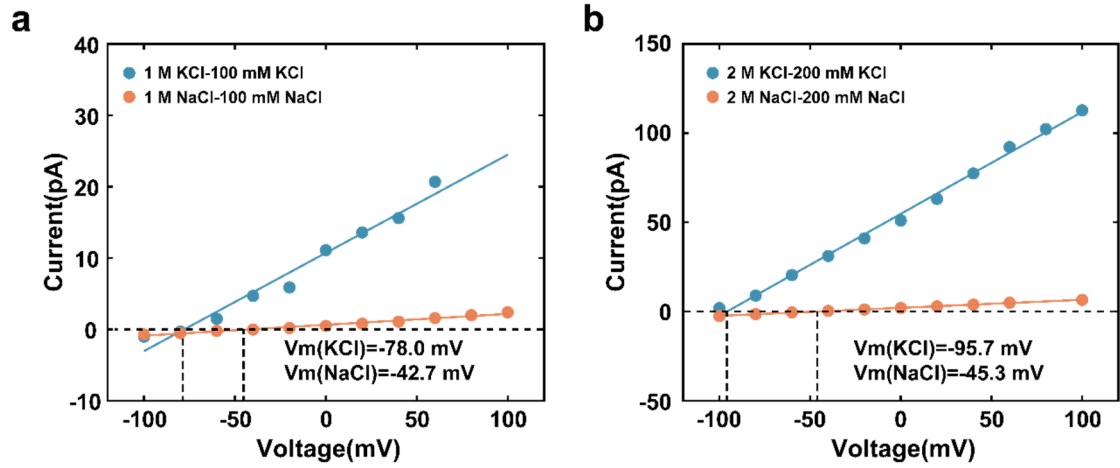


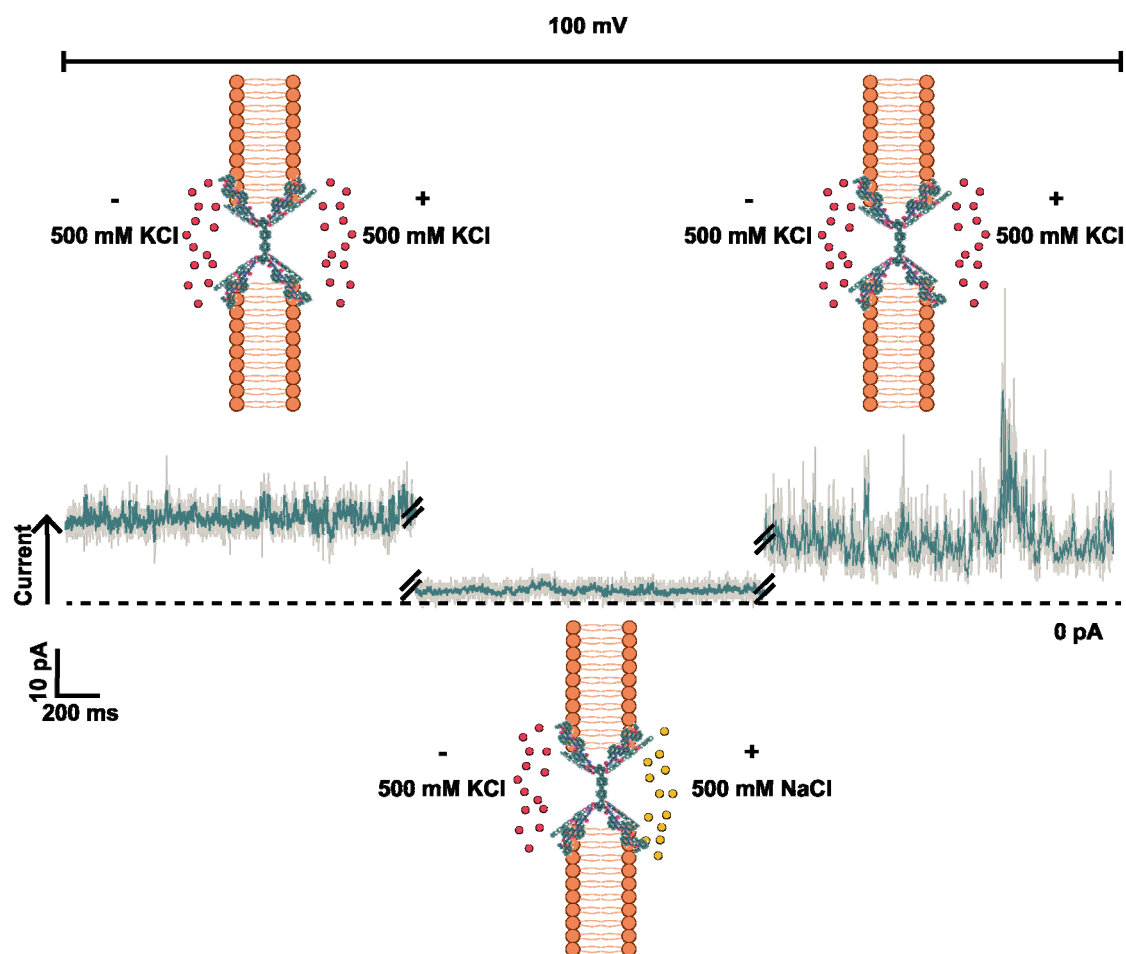
Figure S12. Reversal potential measurements. a-b. I - V curves under ionic concentration gradient in 1 M/100 mM, 2 M/200 mM KCl and NaCl. $V_{\text{rev}} = V_{\text{m}} - V_{\text{redox}}$, V_{m} is the measured voltage, V_{redox} is the redox potential difference. V_{redox} for **a-b.** is -52.9 mV.

Reversal potential measurements: We further demonstrated the ion selectivity of the EPM nanopore by conducting the reversal potential measurements in three groups of asymmetric electrolyte solutions. The ion selectivity is given by the Goldman–Hodgkin–Katz (GHK) equation³⁵

$$V_{\text{rev}} = \frac{k_{\text{B}}T}{e} \ln \left(\frac{S_{\text{GHK}}c_{\text{high}} + c_{\text{low}}}{S_{\text{GHK}}c_{\text{low}} + c_{\text{high}}} \right),$$

where c_{high} and c_{low} are the solution concentrations in the fluid chamber, e is the electron charge, k_{B} is the Boltzmann constant, T is the solution temperature.

In our experimental results, the potassium ion selectivity of the EPM nanopore under asymmetric electrolyte solution (2 M/200 mM) reaches 18.9, close to some of the single-channel selectivity data measured on the natural potassium channel KcsA³⁶⁻³⁹.



SI Fig 13. Current trace of a single EPM nanopore in 500 mM KCl, 500 mM NaCl, 500 mM KCl, respectively.

Reversibility of the experiments: We examined the reversibility of potassium ion selectivity of some EPM nanopores in a solution replacement experiment as shown in **Figure S13**. After EPM formed a stable single channel in 500 mM KCl, we changed the solution of the positive side by using same concentration NaCl solution. The current decrease was then observed (**Figure S13**). We further changed back the solution to KCl solution and the current recovered to the initial state, suggesting the reversibility of potassium selective transport in same EPM pores.

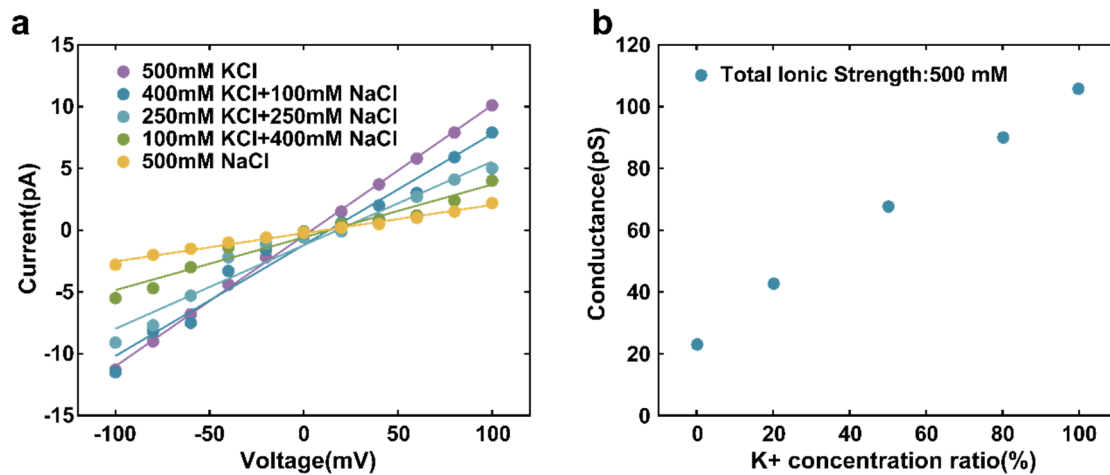


Figure S14. Tuning the selective transport by mole fraction control. **a.** Ionic current measurements in different mixtures of KCl and NaCl solution for a EPM nanopore. The total ionic strength is 500 mM. **b.** Conductance of mixed salt solution as a function of mole fraction of K^+ .

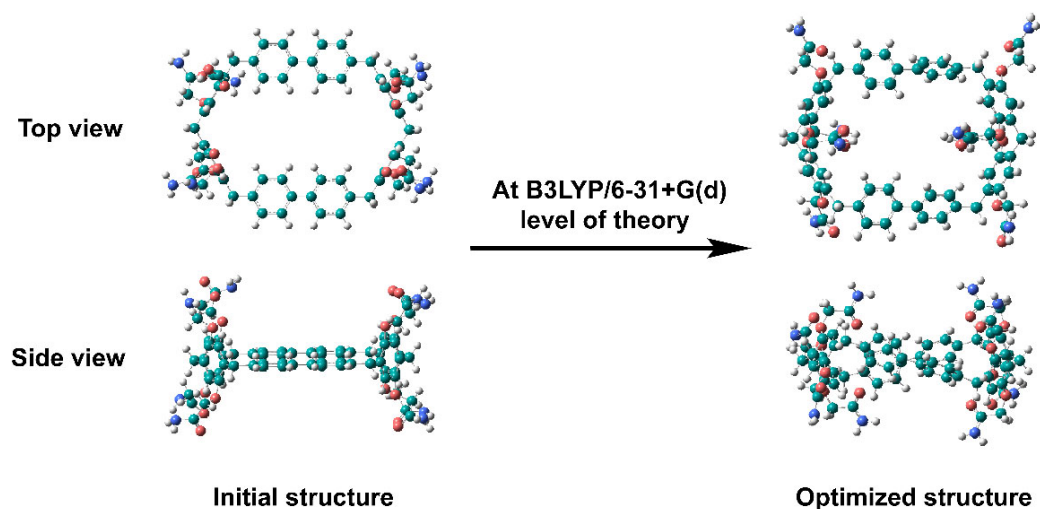


Figure S15. Optimization of EPM conformations using quantum chemistry calculations. The initial structure of the molecule is optimized at B3LYP/6-31+G(d) level of theory using DFT⁴⁰. Considering the crystalized structure¹ may differ from the *in-situ* EPM conformation, we used DFT calculations to infer possible EPM configurations for MD modeling in main **Figure 4**. Since the complete peptide chains were too large to implement, here we used OCH₂CONH₂ as the replacement. The optimized structure shows that the benzene rings prefer to form the erect conformation. The optimized structures and the reported crystalized structure were all implemented in our MD considerations. Our MD simulations suggest that the ion selectivity strongly depends on the atomic conformation of EPM structures, highlighting both rich possibilities of designing new functions using such chemically constructed nanopores and the need of developing novel experimental techniques to probe the aqueous system more precisely.

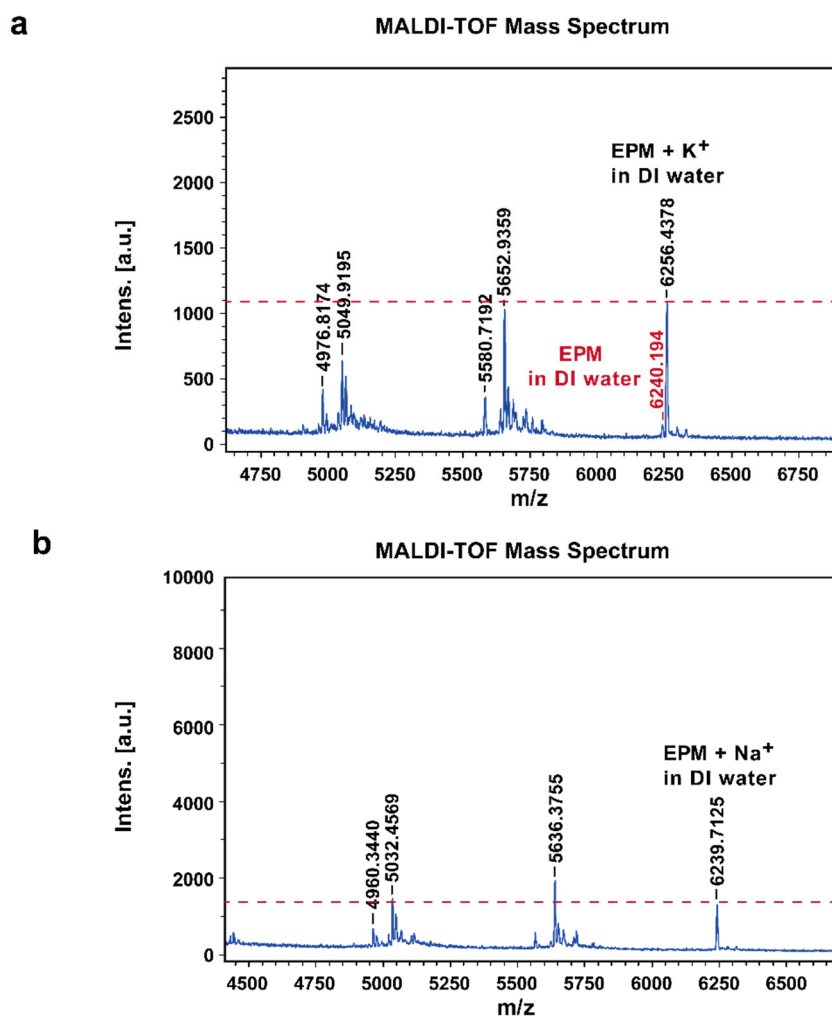
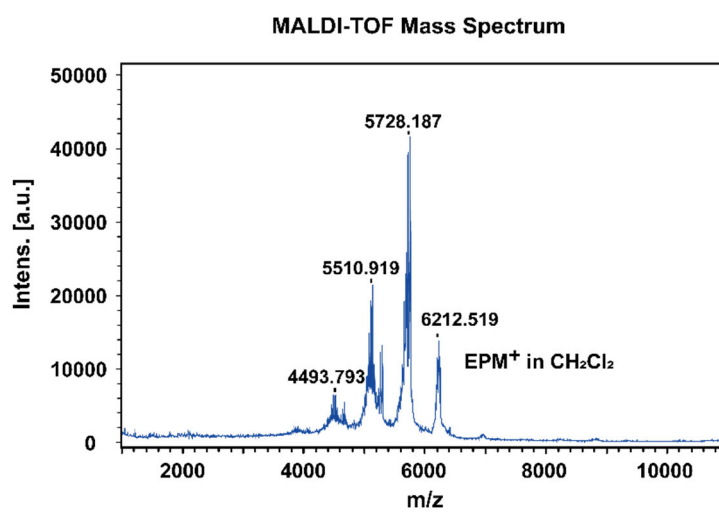


Figure S16. MALDI-TOF mass spectra of the EPM pores in ionic salt solution. a.

A mixture of EPM and 2 M KCl in DI water. Solvent: DI water. **b.** A mixture of EPM

and 2 M NaCl in DI water. Solvent: DI water.

a



b

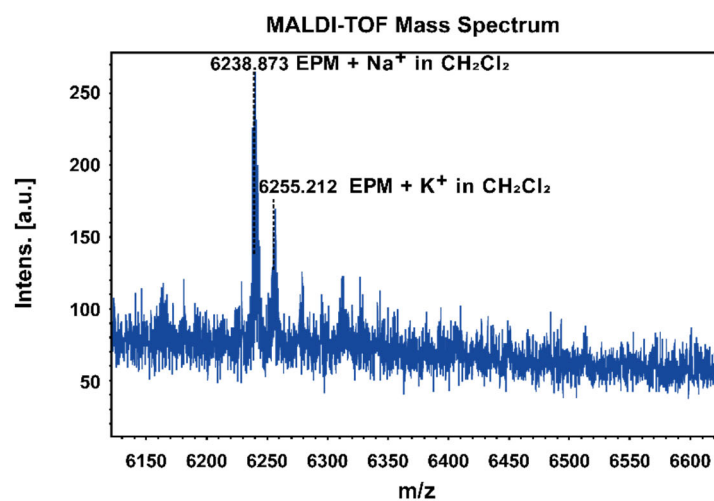


Figure S17. MALDI-TOF mass spectra of the EPM pores in organic salt solution.

a. without and **b.** with addition of KCl and NaCl. Solvent: CH₂Cl₂.

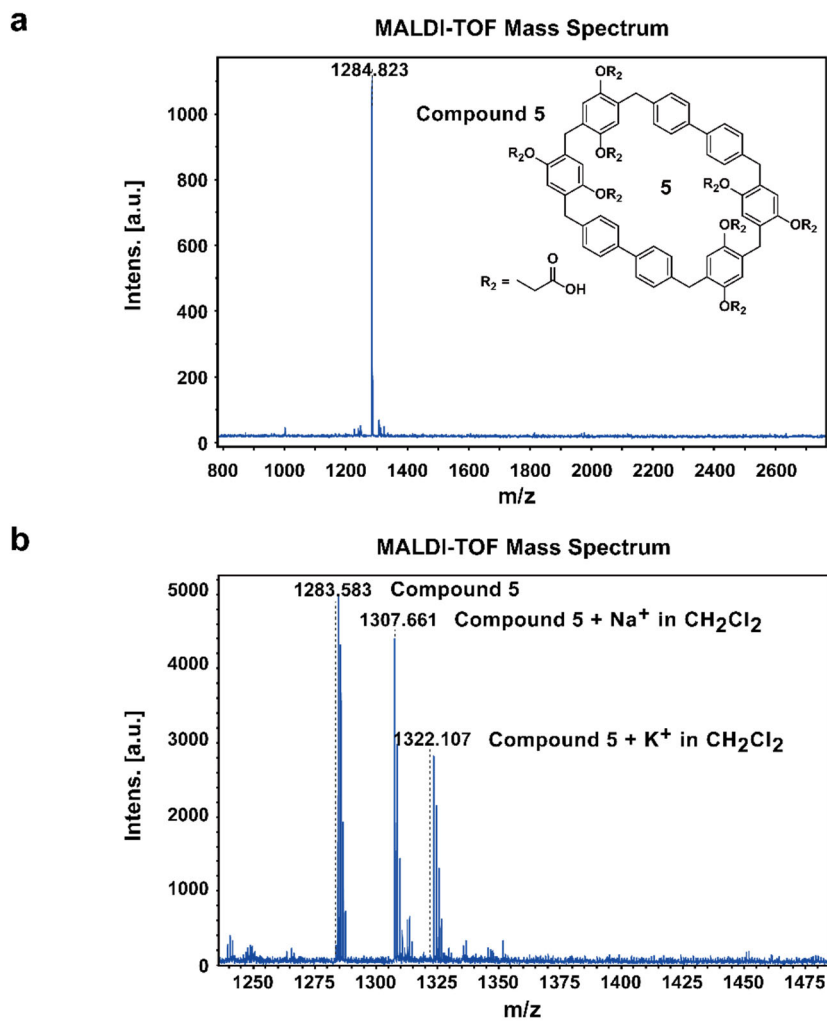


Figure S18. MALDI-TOF mass spectra of the compound **5** **a.** without and **b.** with addition of KCl and NaCl. Solvent: CH₂Cl₂.

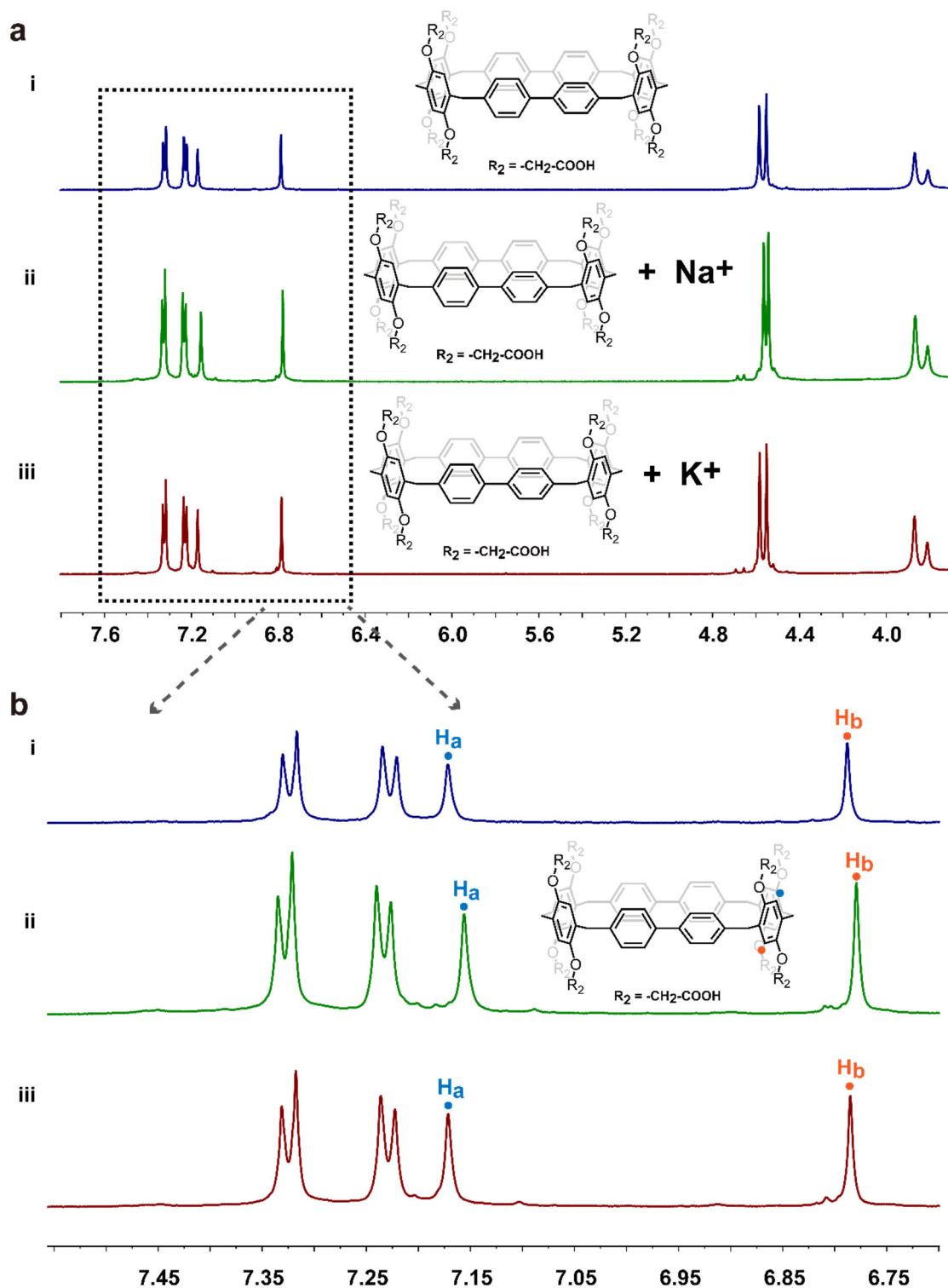


Figure S19. 1H NMR spectra (600 M) **a.** Partial 1H NMR spectra of **i.** compound **5**, **ii.** compound **5** + Na^+ , and **iii.** compound **5** + K^+ in d_6 -DMSO at 298 K. The concentration of compound **5** was 2 mM. **b.** $\Delta\delta_{H_a} = 0.009$ ppm between **i.** and **ii.**; $\Delta\delta_{H_b} = 0.011$ ppm between **i.** and **ii.**

Ion bindings: PMF results from molecular dynamics simulation (main **Figure 4e**) show that the potential well for sodium ions can be deeper than that of potassium ions, suggesting that sodium ions may get tightly trapped in the pore and sodium ions need to overcome a higher energy barrier to translocate through EPM pore than potassium ions. This PMF analysis may capture the observed potassium ion selectivity⁴¹⁻⁴⁴ in EPM nanopores. MALDI-TOF mass spectroscopy and the NMR spectrometry (**Figure S16-19**) can be used to probe the binding between molecules and ions, and the spectral intensity in MALDI-TOF spectra or the chemical shift in ¹H NMR spectra also reflects the strength of the binding degree under the same conditions. As shown in **Figure S16**, when the same concentration of potassium chloride and sodium chloride are added to the aqueous solution of EPM, EPM has binding peaks with both potassium and sodium ions. However, as can be seen from **Figure S16a**, there is also a weak *m/z* peak of EPM on the left of the binding peak of K⁺+EPM, suggesting that EPMs may not all get bound with potassium ion. In **Figure S16b**, the *m/z* peak of only EPM disappears, indicating that EPM is completely bound to sodium ions, and the binding peak intensity is higher than the peak of K⁺+EPM. The NMR result (**Figure S19**) suggests that the binding of Na⁺ ion is preferable to compound **5** than that of K⁺ ion, qualitatively similar to the MD scenario displayed in main **Figure 4e**, which can explain the observed potassium selectivity via a Coulomb blockade mechanism^{45, 46}. MALDI-TOF characterization of ion bindings to compound **5** and compound **6** in organic solution (CH₂Cl₂) shows a similar result (**Figure S17** and **Figure S18**).

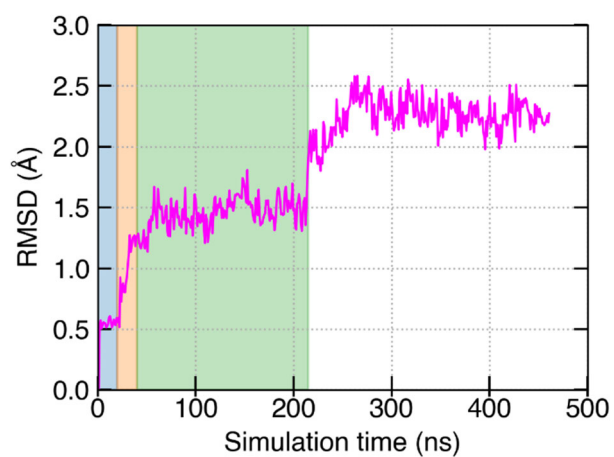
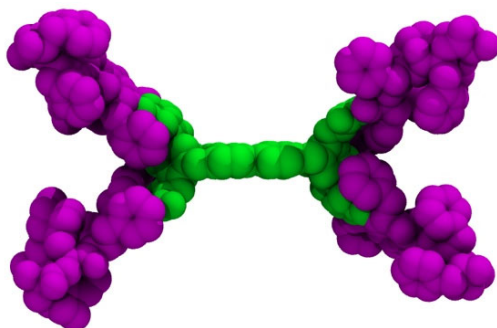
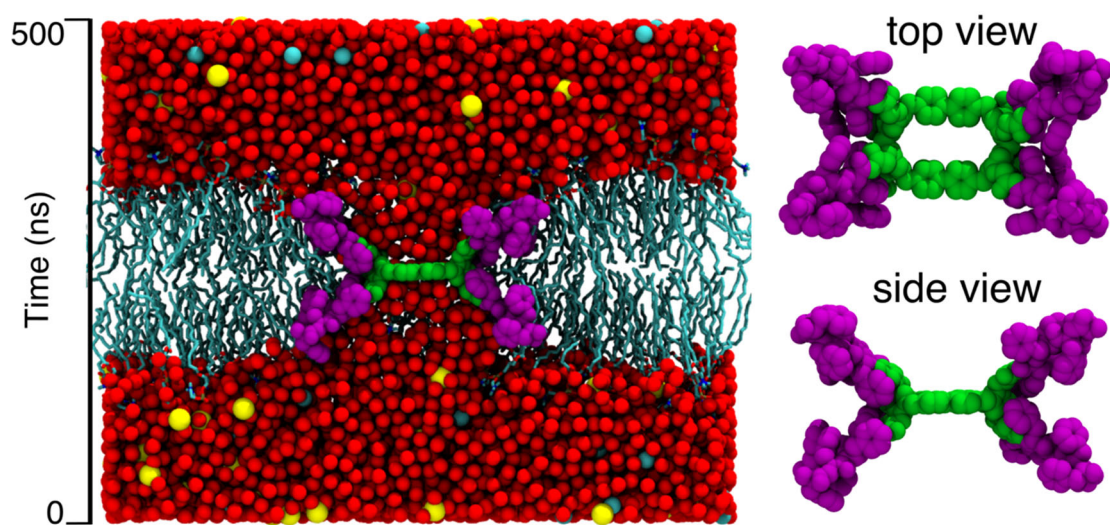


Figure S20. The root-mean-square deviation (RMSD) of the EPM nanopore constriction (excluding the peptide side chains) from its idealized initial conformation as a function of simulation time. The RMSD was computed for all non-hydrogen atoms after aligning each frame to the initial conformation.

6. Supporting movies legends



Supporting Movie 1. A rotating view of the EPM molecule illustrating the 3D structure of the nanopore. The non-hydrogen atoms constituting the constriction region of the nanopore are shown using the green spheres, whereas the Phe side chains are shown using purple spheres.



Supporting Movie 2. All-atom MD simulations of the EPM nanopore embedded in POPC lipid bilayer membrane and solvated in a box of water and ions. The left panel of the movie shows a cut-away view of 0.5 μs long MD simulation trajectory. The oxygen atom of the water molecule is shown using red spheres. The sodium and chlorides ions are shown using yellow and turquoise spheres. The central pillararene molecule is shown via green spheres whereas the Phe side chains are shown using purple spheres. The right panel of the movie simultaneously shows the side and top view of the EPM pore during the MD simulation.

7. Supporting References

1. Gao, B.; Tan, L.-L.; Song, N.; Li, K.; Yang, Y.-W., A high-yield synthesis of [m]biphenyl-extended pillar[n]arenes for an efficient selective inclusion of toluene and m-xylene in the solid state. *Chemical Communications* **2016**, *52* (34), 5804-5807.
2. Chen, L.; Si, W.; Zhang, L.; Tang, G.; Li, Z.-T.; Hou, J.-L., Chiral Selective Transmembrane Transport of Amino Acids through Artificial Channels. *Journal of the American Chemical Society* **2013**, *135* (6), 2152-2155.
3. Shimizu, K.; Mijiddorj, B.; Yoshida, S.; Akayama, S.; Hamada, Y.; ohyama, akifumi; Usui, K.; Kawamura, I.; Kawano, R. De Novo Design of a Nanopore for DNA Detection Incorporating a β -Hairpin Peptide. *ChemRxiv* **2020**. This content is a preprint and has not been peer-reviewed.
4. Mayer, M.; Kriebel, J. K.; Tosteson, M. T.; Whitesides, G. M., Microfabricated Teflon Membranes for Low-Noise Recordings of Ion Channels in Planar Lipid Bilayers. *Biophysical Journal* **2003**, *85* (4), 2684-2695.
5. Gutschmann, T.; Heimburg, T.; Keyser, U.; Mahendran, K. R.; Winterhalter, M., Protein reconstitution into freestanding planar lipid membranes for electrophysiological characterization. *Nature Protocols* **2015**, *10* (1), 188-198.
6. Tunuguntla, R. H.; Allen, F. I.; Kim, K.; Belliveau, A.; Noy, A., Ultrafast proton transport in sub-1-nm diameter carbon nanotube porins. *Nature Nanotechnology* **2016**, *11* (7), 639-644.
7. Sun, K.; Zhao, C.; Zeng, X.; Chen, Y.; Jiang, X.; Ding, X.; Gou, L.; Xie, H.; Li, X.; Zhang, X.; Lin, S.; Dou, L.; Wei, L.; Niu, H.; Zhang, M.; Tian, R.; Sawyer, E.; Yuan, Q.; Huang, Y.; Chen, P.; Zhao, C.; Zhou, C.; Ying, B.; Shi, B.; Wei, X.; Jiang, R.; Zhang, L.; Lu, G.; Geng, J., Active DNA unwinding and transport by a membrane-adapted helicase nanopore. *Nature Communications* **2019**, *10* (1), 5083.
8. Geng, J.; Kim, K.; Zhang, J.; Escalada, A.; Tunuguntla, R.; Comolli, L. R.; Allen, F. I.; Shnyrova, A. V.; Cho, K. R.; Munoz, D.; Wang, Y. M.; Grigoropoulos, C. P.; Ajo-Franklin, C. M.; Frolov, V. A.; Noy, A., Stochastic transport through carbon nanotubes in lipid bilayers and live cell membranes. *Nature* **2014**, *514* (7524), 612-615.
9. Phillips, J. C.; Hardy, D. J.; Maia, J. D.; Stone, J. E.; Ribeiro, J. V.; Bernardi, R. C.; Buch, R.; Fiorin, G.; Hémin, J.; Jiang, W., Scalable molecular dynamics on CPU and GPU architectures with NAMD. *The Journal of Chemical Physics* **2020**, *153* (4), 044130.
10. Batcho, P. F.; Case, D. A.; Schlick, T., Optimized particle-mesh Ewald/multiple-time step integration for molecular dynamics simulations. *The Journal of Chemical Physics* **2001**, *115* (9), 4003-4018.
11. Feller, S. E.; Zhang, Y.; Pastor, R. W.; Brooks, B. R., Constant pressure molecular dynamics simulation: the Langevin piston method. *The Journal of Chemical Physics* **1995**, *103* (11), 4613-4621.
12. Miyamoto, S.; Kollman, P. A., Settle: An analytical version of the SHAKE and RATTLE algorithm for rigid water models. *Journal of Computational Chemistry* **1992**, *13* (8), 952-962.

13. Andersen, H. C., Rattle: A “velocity” version of the shake algorithm for molecular dynamics calculations. *Journal of Computational Physics* **1983**, 52 (1), 24-34.
14. Klauda, J. B.; Venable, R. M.; Freites, J. A.; O’Connor, J. W.; Tobias, D. J.; Mondragon-Ramirez, C.; Vorobyov, I.; MacKerell Jr, A. D.; Pastor, R. W., Update of the CHARMM all-atom additive force field for lipids: validation on six lipid types. *The Journal of Physical Chemistry B* **2010**, 114 (23), 7830-7843.
15. MacKerell Jr, A. D.; Bashford, D.; Bellott, M.; Dunbrack Jr, R. L.; Evanseck, J. D.; Field, M. J.; Fischer, S.; Gao, J.; Guo, H.; Ha, S., All-atom empirical potential for molecular modeling and dynamics studies of proteins. *The Journal of Physical Chemistry B* **1998**, 102 (18), 3586-3616.
16. Vanommeslaeghe, K.; MacKerell Jr, A. D., Automation of the CHARMM General Force Field (CGenFF) I: bond perception and atom typing. *Journal of Chemical Information and Modeling* **2012**, 52 (12), 3144-3154.
17. Yoo, J.; Aksimentiev, A., New tricks for old dogs: improving the accuracy of biomolecular force fields by pair-specific corrections to non-bonded interactions. *Physical Chemistry Chemical Physics* **2018**, 20 (13), 8432-8449.
18. Humphrey, W.; Dalke, A.; Schulten, K., VMD: Visual molecular dynamics. *J. Mol. Graph.* **1996**, 14 (1), 33-38.
19. Case, D. A.; V. Babin; J.T. Berryman; R.M. Betz; Q. Cai; D.S. Cerutti; T.E. Cheatham, I.; T.A. Darden; R.E. Duke; H. Gohlke; A.W. Goetz; S. Gusarov; N. Homeyer; P. Janowski; J. Kaus; I. Kolossváry; A. Kovalenko; T.S. Lee; S. LeGrand; T. Luchko; R. Luo; B. Madej; K.M. Merz; F. Paesani; D.R. Roe; A. Roitberg; C. Sagui; R. Salomon-Ferrer; G. Seabra; C.L. Simmerling; W. Smith; J. Swails; R.C. Walker; J. Wang; R.M. Wolf; X.Wu; Kollman, P. A., AMBER 14, University of California, San Francisco. **2014**.
20. Jo, S.; Kim, T.; Iyer, V. G.; Im, W., CHARMM-GUI: a web-based graphical user interface for CHARMM. *Journal of Computational Chemistry* **2008**, 29 (11), 1859-1865.
21. Jorgensen, W. L.; Chandrasekhar, J.; Madura, J. D.; Impey, R. W.; Klein, M. L., Comparison of simple potential function for simulating liquid water. *Journal of Chemical Physics* **1983**, 79 (2), 926-935.
22. Grubmüller, H.; Heymann, B.; Tavan, P., Ligand binding: molecular mechanics calculation of the streptavidin-biotin rupture force. *Science* **1996**, 271 (5251), 997-999.
23. Isralewitz, B.; Izrailev, S.; Schulten, K., Binding pathway of retinal to bacterio-opsin: a prediction by molecular dynamics simulations. *Biophysical Journal* **1997**, 73 (6), 2972.
24. Kumar, S.; Rosenberg, J. M.; Bouzida, D.; Swendsen, R. H.; Kollman, P. A., The weighted histogram analysis method for free-energy calculations on biomolecules. I. The method. *Journal of Computational Chemistry* **1992**, 13 (8), 1011-1021.
25. Si, W.; Li, Z.-T.; Hou, J.-L., Voltage-Driven Reversible Insertion into and Leaving from a Lipid Bilayer: Tuning Transmembrane Transport of Artificial Channels. *Angewandte Chemie International Edition* **2014**, 53 (18), 4578-4581.
26. Cao, C.; Liao, D. F.; Yu, J.; Tian, H.; Long, Y. T., Construction of an aerolysin nanopore in a lipid bilayer for single-oligonucleotide analysis. *Nat Protoc* **2017**, 12 (9),

1901-1911.

27. Feng, J.; Graf, M.; Liu, K.; Ovchinnikov, D.; Dumcenco, D.; Heiranian, M.; Nandigana, V.; Aluru, N. R.; Kis, A.; Radenovic, A., Single-layer MoS₂ nanopores as nanopower generators. *Nature* **2016**, *536* (7615), 197-200.
28. Tabard-Cossa, V.; Trivedi, D.; Wiggin, M.; Jetha, N. N.; Marziali, A., Noise analysis and reduction in solid-state nanopores. *Nanotechnology* **2007**, *18* (30), 305505.
29. Fragasso, A.; Schmid, S.; Dekker, C., Comparing Current Noise in Biological and Solid-State Nanopores. *ACS Nano* **2020**, *14* (2), 1338-1349.
30. Lang, C.; Deng, X.; Yang, F.; Yang, B.; Wang, W.; Qi, S.; Zhang, X.; Zhang, C.; Dong, Z.; Liu, J., Highly Selective Artificial Potassium Ion Channels Constructed from Pore-Containing Helical Oligomers. *Angewandte Chemie International Edition* **2017**, *56* (41), 12668-12671.
31. Chen, F.; Shen, J.; Li, N.; Roy, A.; Ye, R.; Ren, C.; Zeng, H., Pyridine/Oxadiazole-Based Helical Foldamer Ion Channels with Exceptionally High K⁺/Na⁺ Selectivity. *Angewandte Chemie International Edition* **2020**, *59* (4), 1440-1444.
32. Jeon, Y. J.; Kim, H.; Jon, S.; Selvapalam, N.; Oh, D. H.; Seo, I.; Park, C.-S.; Jung, S. R.; Koh, D.-S.; Kim, K., Artificial Ion Channel Formed by Cucurbit[n]uril Derivatives with a Carbonyl Group Fringed Portal Reminiscent of the Selectivity Filter of K⁺ Channels. *Journal of the American Chemical Society* **2004**, *126* (49), 15944-15945.
33. Tanaka, Y.; Kobuke, Y.; Sokabe, M., A Non-Peptidic Ion Channel with K⁺ Selectivity. *Angewandte Chemie International Edition in English* **1995**, *34* (6), 693-694.
34. Kobuke, Y.; Ueda, K.; Sokabe, M., Artificial non-peptide single ion channels. *Journal of the American Chemical Society* **1992**, *114* (20), 7618-7622.
35. Hille, B., Chapter 14 Selective permeability: Independence. In *Ion Channels of Excitable Membranes Third Edition*, Sinauer Associates: 2001; pp 445-450.
36. Schrempf, H.; Schmidt, O.; Kümmerlen, R.; Hinnah, S.; Müller, D.; Betzler, M.; Steinkamp, T.; Wagner, R., A prokaryotic potassium ion channel with two predicted transmembrane segments from *Streptomyces lividans*. *The EMBO Journal* **1995**, *14* (21), 5170-5178.
37. Meuser, D.; Splitt, H.; Wagner, R.; Schrempf, H., Exploring the open pore of the potassium channel from *Streptomyces lividans*. *FEBS Letters* **1999**, *462* (3), 447-452.
38. LeMasurier, M.; Heginbotham, L.; Miller, C., KcsA: It's a Potassium Channel. *Journal of General Physiology* **2001**, *118* (3), 303-314.
39. Shrivastava, I. H.; Peter Tieleman, D.; Biggin, P. C.; Sansom, M. S. P., K⁺ versus Na⁺ Ions in a K Channel Selectivity Filter: A Simulation Study. *Biophysical Journal* **2002**, *83* (2), 633-645.
40. Frisch, M. J.; Trucks, G. W.; Schlegel, H. B.; Scuseria, G. E.; Robb, M. A.; Cheeseman, J. R.; Scalmani, G.; Barone, V.; Petersson, G. A.; Nakatsuji, H.; Li, X.; Caricato, M.; Marenich, A. V.; Bloino, J.; Janesko, B. G.; Gomperts, R.; Mennucci, B.; Hratchian, H. P.; Ortiz, J. V.; Izmaylov, A. F.; Sonnenberg, J. L.; Williams; Ding, F.; Lipparini, F.; Egidi, F.; Goings, J.; Peng, B.; Petrone, A.; Henderson, T.; Ranasinghe, D.; Zakrzewski, V. G.; Gao, J.; Rega, N.; Zheng, G.; Liang, W.; Hada, M.; Ehara, M.; Toyota, K.; Fukuda, R.; Hasegawa, J.; Ishida, M.; Nakajima, T.; Honda, Y.; Kitao, O.;

- Nakai, H.; Vreven, T.; Throssell, K.; Montgomery Jr., J. A.; Peralta, J. E.; Ogliaro, F.; Bearpark, M. J.; Heyd, J. J.; Brothers, E. N.; Kudin, K. N.; Staroverov, V. N.; Keith, T. A.; Kobayashi, R.; Normand, J.; Raghavachari, K.; Rendell, A. P.; Burant, J. C.; Iyengar, S. S.; Tomasi, J.; Cossi, M.; Millam, J. M.; Klene, M.; Adamo, C.; Cammi, R.; Ochterski, J. W.; Martin, R. L.; Morokuma, K.; Farkas, O.; Foresman, J. B.; Fox, D. J. *Gaussian 16 Rev. B.01*, Wallingford, CT, 2016.
41. Sahu, S.; Elenewski, J.; Rohmann, C.; Zwolak, M., Optimal transport and colossal ionic mechano-conductance in graphene crown ethers. *Science Advances* **2019**, *5* (7), eaaw5478.
42. Liu, J.; Li, F.; Wang, Y.; Pan, L.; Lin, P.; Zhang, B.; Zheng, Y.; Xu, Y.; Liao, H.; Ko, G.; Fei, F.; Xu, C.; Du, Y.; Shin, K.; Kim, D.; Jang, S.-S.; Chung, H. J.; Tian, H.; Wang, Q.; Guo, W.; Nam, J.-M.; Chen, Z.; Hyeon, T.; Ling, D., A sensitive and specific nanosensor for monitoring extracellular potassium levels in the brain. *Nature Nanotechnology* **2020**, *15* (4), 321-330.
43. MacKinnon, R., Potassium Channels and the Atomic Basis of Selective Ion Conduction (Nobel Lecture). *Angewandte Chemie International Edition* **2004**, *43* (33), 4265-4277.
44. Ulmschneider, M. B.; Bagn eris, C.; McCusker, E. C.; DeCaen, P. G.; Delling, M.; Clapham, D. E.; Ulmschneider, J. P.; Wallace, B. A., Molecular dynamics of ion transport through the open conformation of a bacterial voltage-gated sodium channel. *Proceedings of the National Academy of Sciences* **2013**, *110* (16), 6364.
45. Chen, F.; Gu, Z.; Zhao, C.; Chen, Y.; Jiang, X.; He, Z.; Lu, Y.; Zhou, R.; Feng, J., Ionic conductance oscillations in sub-nanometer pores probed by optoelectronic control. *Matter* **2021**, *4*, 1-14.
46. Berezhkovskii, A. M.; Bezrukov, S. M., Optimizing transport of metabolites through large channels: molecular sieves with and without binding. *Biophysical Journal* **2005**, *88* (3), L17-L19.